Polymer-solubilized structure of the mechanosensitive channel MscS suggests the role of protein-lipid interactions in the functional gating cycle

Elissa Moller [1,2,3], Madolyn Britt [2,3], Fei Zhou [1], Hyojik Yang[5], Robert Ernst [5], Sergei Sukharev [2,3,4,#], Doreen Matthies [1,#]

[1] Unit on Structural Biology, Division of Basic and Translational Biophysics, *Eunice Kennedy Shriver* National Institute of Child Health and Human Development, National Institutes of Health, Bethesda, MD, USA.

[2] Biophysics Graduate Program, University of Maryland, College Park, MD, USA.
[3] Department of Biology, University of Maryland, College Park, MD, USA.
[4] Institute for Physical Science and Technology, University of Maryland, College Park, MD, USA.
[5] Department of Microbial Pathogenesis, University of Maryland, Baltimore, MD, USA.
[6] Biochemistry and Molecular Biology, University of Texas Medical School, Houston, TX, USA.

Correspondence to Sergei Sukharev (sukharev@umd.edu) and Doreen Matthies (Doreen.Matthies@nih.gov)

Abstract

Membrane protein structure determination is not only technically challenging but is further complicated by the removal or displacement of lipids, which can result in non-native conformations or a strong preference for certain states at the exclusion of others. This is especially applicable to mechanosensitive channels (MSC's) that evolved to gate in response to subtle changes in membrane tension, such as MscS, a model bacterial system for MSC gating with homologs found across all phyla of walled organisms. MscS is highly adaptive, it readily opens under super-threshold tension but under lower tensions it inactivates and can only recover when tension is released. Functional data strongly suggests a restructuring of the protein-lipid boundary during the slow inactivation and recovery processes. Existing cryo-EM structures fall into two categories depending on the method of solubilization: (1) non-conductive (lipid-reconstituted or mixed micelles) characterized by kinked pore-lining helices and splayed lipid-facing helices, or (2) semi-open (pure detergent or short-chain lipids). These structures do not explain the full functional gating cycle consisting of three well defined states: open, closed, and inactivated. Here, we present a 3 Å MscS structure in native nanodiscs generated with Glyco-DIBMA polymer solubilization which eliminates the lipid removal step common to all previous structures. Besides the protein in the splayed conformation, we observe well-resolved densities that represent phospholipids intercalating between the lipid-facing and pore-lining helices in preferred orientations. The structure illustrates the lipid-based mechanism for the uncoupling of the tension sensing helical pairs from the gate and prompts critical questions on whether the two distinct tension driven opening-closing and inactivation-recovery pathways are separated by the kinetic principle and what types of forces drive the recovery back to a more compact closed state.

Introduction

MscS is an essential low threshold osmolyte release valve that was first identified in bacteria but can be found in all walled cells for regulating turgor pressure, surviving osmotic shock, and providing environmental stability. *Escherichia coli* MscS is a homo-heptamer, comprising three transmembrane helices and a soluble cytoplasmic domain found in the inner membrane. It forms a highly adaptive mechanosensitive channel (MSC) with three discrete functional states: open, closed, and inactivated. There are two separate opening and inactivation pathways, both originating from the closed state. Each pathway is characterized by its own tension sensitivity, in-plane protein area expansion, and kinetics. The inactivation and recovery transitions are slow and sensitive to the lipid-anchoring sidechains. While there are many *E. coli* MscS structures (Angiulli et al., 2020; Bass et al., 2002; Flegler et al., 2021; Park et al., 2023; Rasmussen et al., 2019a; Reddy et al., 2019; Wang et al., 2008; Zhang et al., 2021), they do not explain the full three-state functional cycle. There are two overarching classes of structures: a splayed non-conductive state and an expanded semi-conductive state. These protein conformations are highly dependent on the surrounding lipid environment and the solubilizing conditions with high detergent concentrations yielding the semi-conductive state and the presence of lipids resulting in the splayed non-conductive state. The lipidation of the channel causes a large rearrangement of the transmembrane helices and can be induced simply by adding lipids to form a mixed micelle rather than pure detergent (Flegler et al., 2021). This structure overlays quite well with the nanodisc structures using full-length lipids (Rasmussen et al., 2019a; Reddy et al., 2019). Using artificially short acyl chains can result in a structure more similar to the semi-conductive state (Park et al., 2023; Zhang et al., 2021).
There are many speculations on the role of lipids in the MscS gating mechanism. Previous data have shown that MscS opens with slightly different tension sensitivities when comparing the more native spheroplast lipid environments to reconstitution in soybean lipids (Belyy et al., 2010b; Sukharev, 2002). While MscS opens robustly in most tested environments, the slow inactivation process and its dependence on the lipid anchoring residues suggests that lipids may be an inseparable part of MscS inactivation.

Direct membrane disruption via polymer solubilization to form native nanodiscs was first shown for styrene maleic acid (SMA) (Knowles et al., 2009) and widely used for functional studies prior to its use for high-resolution cryo-EM reconstruction of Alternative complex III (Sun et al., 2018) and AcrB (Qiu et al., 2018). Many different polymers are now commercially available; the polymers used in this study are Glyco-DIBMA (Danielczak et al., 2022), SMALP 200 (Knowles et al., 2009), and CyclAPol (Higgins et al., 2021). Glyco-DIBMA is a diisobutylene-maleic acid polymer with an additional glycosylation, SMALP is a poly-styrene-maleic anhydride polymer with hydrophobic styrene groups and reactive, functionalizable anhydrides, and CyclAPol is a cycloalkane-modified amphiphilic polymer.

In the present work we solve the structure of MscS in Glyco-DIBMA to 3 Å using single-particle cryo-EM and identify specific positions and conformations of lipids intercalating between the lipid-facing TM1-TM2 helical pairs and the gate-forming TM3s. The importance of TM2-TM3 interactions for proper MscS gating has been suggested previously (Belyy et al., 2010a). The identified lipids likely work as a 'filler' uncoupling the gate from the peripheral helices thus interrupting the tension transmission route. We discuss the functional state represented by the MscS-lipid complex, the mechanistic role of the intercalated lipids, spatial characteristics of the system, physical forces acting on the protein-lipid complex, and the place of this structure in the network of conformational pathways describing the functional cycle of MscS.

Methods

MscS Expression and Inner Membrane Isolation

E. coli MscS WT was expressed in MJF465 cells (Frag1 ΔmscL::Cm, ΔyggB, ΔmscK::kan) (Levina et al., 1999) from the pB10d vector, a modified pB10b plasmid (Iscla et al., 2008). The plasmid is IPTG inducible with the lac UV5 and lacIq promoters, confers ampicillin resistance, and includes a C-terminal 6-His tag on the MscS gene. It uses the high-copy-number ColE1/pMB1/pBR322/pUC origin of replication and the T7 bacteriophage ribosome binding site. The MJF465 strain originated from the I. Booth laboratory (University of Aberdeen, Aberdeen, UK) and was provided by Dr. Samantha Miller (University of Aberdeen). A single colony of the plasmid containing strain was inoculated into 35 mL Luria Bertani (LB) media supplemented with Ampicillin (Amp) and grown overnight. 5 mL of the overnight culture was sub-cultured into 6 2-L flasks containing 1 L LB supplemented with Amp and grown for 2 hours shaking 225 rpm at 30ºC before induction with 1 mM IPTG for an additional 3 hours to a final OD600 of 2.0. When the target OD was achieved cells were placed on ice to prevent further growth, pelleted at 4ºC, and resuspended in French Press Buffer (150 mM NaCl, 20 mM Tris pH 7.6) supplemented with lysozyme and PMSF to 30 mL total volume before rupturing with a French press. Unbroken cells were pelleted by centrifugation at 10K for 15 min at 4ºC, supernatant was then ultracentrifuged at 25K for 1 hr at 4ºC to pellet membranes. Supernatant was discarded and membranes were resuspended in Resuspension Buffer (20% [w:v] sucrose, 5 mM EDTA) and homogenized before being placed on top of a 3 step sucrose gradient of 0.77 M, 1.44 M, and 2.02 M prepared in Gradient Buffer (5 mM EDTA, 20 mM HEPES pH 7.2) and ultracentrifuged at 25K for 16 hrs at 8ºC. The inner membranes were harvested from the upper band of the gradient by puncturing the tube wall with a syringe needle, diluted in Gradient Buffer with no sucrose to 70 mL total volume, and ultracentrifuged at 25K for 1 hr at 4ºC to re-pellet membranes. The membrane pellets were stored at -80ºC until use.

Glyco-DIBMA Solubilization and Affinity Purification

E. coli inner membranes were resuspended to 5% [w:v] in Glyco-DIBMA Buffer (100 mM NaCl, 20 mM HEPES pH 7.4) and homogenized before the addition of 0.5% [w:v] of solid Glyco-DIBMA (Cube Biotech). The first condition (Glyco-DIBMA #1) was allowed to solubilize overnight at 4ºC on the rotisserie while the second condition (Glyco-DIBMA #2) was allowed to solubilize for 2 hrs at room temperature on the rotisserie. The insoluble fraction was then pelleted by ultracentrifugation at 25K for 35 min at 4ºC. The supernatant was then diluted 1:5 to improve binding efficiency and incubated overnight on the rotisserie at 4ºC with TALON Cobalt Resin (Takara Bio). The next day the resin was washed with 10 column volumes of Glyco-DIBMA Buffer, 10 column volumes of 10 mM imidazole Column Buffer (10% glycerol [v:v], 100 mM NaCl, 20 mM HEPES pH 7.4), 5 column volumes of 20 mM imidazole Column Buffer, and 5 column volumes of 40 mM imidazole Column Buffer before elution with 350 mM imidazole Column Buffer. Elution fractions were then dialyzed with Glyco-DIBMA Buffer overnight to remove imidazole and glycerol and concentrated the following day using a 100 kDa ultrafiltration membrane (Amicon) to desired concentration for cryo-EM grid preparation.

SMALP Solubilization and Affinity Purification

E. coli inner membranes were resuspended to 20 mg/mL in SMALP Buffer (10% glycerol [v:v] 500 mM NaCl, 50 mM Tris pH 8.0) and homogenized before the addition of 1% [w:v] of SMALP 200 (Orbiscope) and allowed to solubilize for 2 hrs at room temperature on the rotisserie. SMALP 300 was also attempted but did not successfully solubilize. The insoluble fraction was then pelleted by ultracentrifugation at 25K for 35 min at 4ºC. The supernatant was then diluted 1:4 to improve binding efficiency and incubated overnight on the rotisserie at 4ºC with TALON Cobalt Resin (Takara Bio). The next day the resin was washed with 10 column volumes of SMALP Buffer and 10 column volumes of 20 mM imidazole SMALP Buffer before elution with 300 mM imidazole SMALP Buffer. Elution fractions were then dialyzed with Purification Buffer (5% glycerol [v:v] 250 mM NaCl, 20 mM Tris pH 8.0) overnight to remove imidazole

and concentrated the following day using a 100 kDa ultrafiltration membrane (Amicon) to desired concentration for cryo-EM grid preparation.

CyclAPol Solubilization and Affinity Purification
E. coli inner membranes were resuspended to 10 mg/mL in Purification Buffer and homogenized before the addition of 0.1% [w:v] of CyclAPol C_8-C_0-50 and allowed to solubilize for 2 hrs at room temperature on the rotisserie. CyclAPol C_8-C_0-50 was a provided by Manuela Zoonens (Université de Paris and Institut de Biologie Physico-Chimique, Paris, France) and is now commercially available as Ultrasolute Amphipol 18 (Cube Biotech). The insoluble fraction was then pelleted by ultracentrifugation at 25K for 35 min at 4ºC and the supernatant was incubated overnight on the rotisserie at 4ºC with TALON Cobalt Resin (Takara Bio). The next day the resin was washed with 10 column volumes of Purification Buffer and 10 column volumes of 10 mM imidazole Purification Buffer before elution with 300 mM imidazole Purification Buffer. Elution fractions were then dialyzed with Purification Buffer overnight to remove imidazole and concentrated the following day using a 100 kDa ultrafiltration membrane (Amicon) to desired concentration for cryo-EM grid preparation.

Protein Validation using SDS-PAGE, Western Blot, and BN-Page.
The protein fractions were resolved and analyzed using SDS-PAGE, Western Blot, and BN-PAGE. For SDS-PAGE samples were prepared with 4X Bolt LDS Sample Buffer (Invitrogen) and placed on a heat at 80°C for 10 minutes before loading into 4-12% Bis-Tris gel (Invitrogen) with NuPAGE MOPS SDS Buffer (Invitrogen) and running at 80 V for 15 minutes followed by 200 V for 45 minutes. Gel was fixed and then stained with Colloidal Blue Stain (Invitrogen) overnight and de-stained in water and scanned the following day.. For Western Blot SDS-PAGE gel was transferred to PVDF membrane at 30 V for 45 min in NuPAGE Transfer Buffer (Invitrogen) and blocked with 4% BSA in TTBS [100 mM Tris pH 7.5, 150 mM NaCl, 0.1% Tween 20] for 1 hour, stained with 0.1 µg/mL Anti-6X His tag antibody (abcam) in 2% BSA in TTBS for 1 hour, washed with TTBS and imaged with ChemiDoc (BioRad) using WesternBright (advansta). For BN-PAGE samples were prepared with NativePAGE Sample Buffer and 0.125% NativePAGE G-250 Sample Additive (Invitrogen) and loaded into a 4-16% Bis-Tris gel (Invitrogen) with NativePAGE Running Buffer and NativePAGE Cathode Bufffer in the inner chamber (Invitrogen) before running at 150 V for 1 hour followed by 250 V for 1 hour. Gel was fixed in 40% ethanol, 10% acetic acid microwaved for 1 minute and then stained with Colloidal Blue Stain (Invitrogen) overnight and de-stained in water and scanned the following day. Gel images and Western Blots for each purification can be found in Supplemental Figures 3-5.

Negative Staining Electron Microscopy
3 µL of MscS was applied on a glow discharged carbon coated 400 square mesh copper grid (EMS) and incubated for 1 min. The grid was then blotted by filter paper (Whatman) and washed once with 3 µL of Nano-W negative staining solution (Nanoprobes) followed by incubation with 3 µL of Nano-W for 1 min. The grid was blotted to remove excess staining solution and air-dried by waving. Images were recorded using an FEI Tecnai T20 TEM operated at 200 kV with a direct electron detector K2 Summit (Gatan Inc). Data was collected using SerialEM (Mastronarde, 2005) at a nominal magnification of 25,000x, and a defocus range between -1.3 and -2. Collection parameters specific to each dataset are listed in the legends of Supplemental Figures 3-5. Image processing was performed using cisTEM v1.0.0. (Grant et al., 2018).

Cryo-EM Grid Preparation and Data Collection
3 µl of purified MscS was applied to a glow-discharged R 1.2/1.3 400 Cu mesh + 2nm C grid (Quantifoil). The grids were blotted for 6 s at 4 °C and 95% humidity, and plunge-frozen into liquid ethane using a Leica EM GP2 (Leica) and stored in liquid nitrogen. The grids were screened on an FEI Tecnai T20 TEM before data collection. Cryo-EM datasets were acquired with SerialEM (Mastronarde, 2005) using a Titan Krios (FEI, now ThermoFisher Scientific) operated at 300 kV and equipped with an energy filter and K3 camera (Gatan Inc.). Movies of 50-60 frames were collected with a total dose of 50

e-/Å^2 were recorded with a nominal magnification of 105,000x corresponding to a physical pixel size of 0.83-0.85 Å/px at a dose rate of 9-15 e-/px/s and a defocus range of -0.8 to -1.8 µm. Specific collection parameters for each dataset can be found in Supplemental Table 1.

Cryo-EM Data Processing

The specific workflows for image processing are illustrated in Supplemental Figures 6-10. All processing was performed within cryoSPARC v3.3.250 (Punjani et al., 2017). Movies were processed with patch motion correction (Zheng et al., 2017) and patch CTF estimation (Rohou and Grigorieff, 2015). Blob picker was used for the majority of particle picking and particles were extracted with a box size of 320-360 Å and subjected to 2D classification to remove junk particles. Selected particles were used for ab-initio reconstruction, heterogeneous refinement, and non-uniform refinement (Punjani et al., 2020).

Model Building and Refinement

For the MscS atomic model, PDB 7ONL (Flegler et al., 2021) was rigid-body fitted into the filtered map using UCSF ChimeraX v.1.6.1. The model was then manually rebuilt in COOT v.0.8.9.2 using the filtered map, which was generated from non-uniform refinement with C7 applied. Iterative rounds of manual refinement in COOT and real-space refinement in Phenix v.1.20.1-4487 (Liebschner et al., 2019) were performed. The quality of the model and fit to the density was assessed using MolProbity55 and Phenix54. All structural figures were prepared using UCSF ChimeraX v.1.6. Cryo-EM map and model analysis values are listed in Supplemental Table 2. PDBs have been made available together with the cryo-EM maps with the following PDB IDs:

Lipid Mass Spectrometry

The remaining protein sample from Glyco-DIBMA #2 was used for Mass Spectrometry Lipid Analysis along with a control of purified *E. coli* inner membranes. 1 µL of sample pellet was scraped and plated directly to a steel re-usable MALDI plate. 1 µL of 70% citric acid extraction buffer was spotted on top of the plated sample. The steel MALDI plate was added to chamber with water on bottom and placed in 110-degree Celsius oven for 30 minutes. After, the plate was rinsed with water and air dried. 1 µL of Norharmane matrix was spotted on each sample. A Bruker Matrix-Assisted Laser Desorption/Ionization trapped ion mobility spectrometry Time-of-Flight Mass Spectrometry MALDI (tims TOF) MS was used for FLAT (direct biomass MS for visualization of lipid A and phospholipids) and direct analysis. This MALDI (tims TOF) MS is equipped with a dual ESI/MALDI source with a SmartBeam3D 10 kHz frequency tripled Nd:YAG laser (355 nm); the system was operated in "qTOF" mode (TIMS deactivated) for these experiments. Ion transfer tuning was used with the following parameters: funnel1 RF, 440.0 Vpp; funnel2 RF,490.0 Vpp; multipole RF, 490.0 Vpp; CID energy, 0.0 eV; and deflection delta,−60.0V. Quadrupole was used with the following values for MS mode: ion energy,4.0 eV. Them/z scan range for MS is set to 1000 to 3000. Collision cell activation of ions used the following values for MS mode: collision energy, 9.0 eV; collision RF, 3900.0Vpp. In the MS/MS mode, the precursor ion was chosen by typing the targeted m/z value including two digits to the right of the decimal point. Typical isolation width and collision energy were set to 4−6 m/z and 100−110 eV, respectively. FocusPre TOF used the following values for transfer time, 110.0µs, and prepulsestorage, 9.0µs. Agilent ESI tune mix was used to perform calibration of them/z scale. MALDI parameters in qTOF were optimized to maximize intensity by tuning ion optics, laser intensity, and laser focus. All spectra were collected at a 104µm laser diameter with beam scan on using 800 laser shots per spot and 70 and 80% laser power, respectively. MS data were collected in negative ion mode. In all cases,10 mg/mL of norharmane (NRM) in 1:2 MeOH/CHCl3 [v:v] was used for lipid detection. All MALDI (tims TOF) MS were visualized using mMass (Ver 5.5.0). Peak picking was conducted in mMass using the following parameters: S/N threshold: 3.0; relative intensity threshold: 5.0%; picking height: 50; apply baseline and smoothing.

Results

Cryo-EM of E. coli MscS in native nanodiscs
Using Glyco-DIBMA polymer solubilization to form native nanodiscs yielded a successful 3D reconstruction (Figure 1). A selection of the 2D class averages used for the 3D reconstruction are shown in Figure 1A. The overall map resolution is 2.99 Å with the highest resolution in the cytoplasmic domain reaching 2.6 Å (Figure 1B). Side chain densities for a helix and beta sheet are shown in Supplemental Figure 11. At this resolution the protein was modelled from residue 17 to 281 (Figure 1C).

Additional densities unaccounted for by the modelled protein were examined and some of them were modelled as lipids. These densities are shown in Figure 2. Lipid 1 (Figure 2D) is oriented parallel to the bilayer outer leaflet between the TM2's of neighboring chains. Lipids 2-4 (Figure 2E-G) are oriented perpendicular to the bilayer inner leaflet between the loops connecting TM1 and TM2 of neighboring chains. These lipids are shown in C1 symmetry alongside remaining unmodelled densities in Supplemental Figure 12, a full list of nearby residues is given in Supplemental Table 3.

Assigning lipids to POPE or POPG? Currently modelled as POPE based solely on the fact that it's more prevalent in the bilayer and there was not a significant increase in POPG in Mass Spec (Figure 3, Table 1), arguably an increase in POPE but we'd need more replicates to confidently claim that

Mass-spectrometry of co-purified lipids and comparison with the inner membrane composition
(text)

Analysis of residues coordinating lipids in MscS crevices

Charged/Polar/Pi residues nearby – with the presence of a + charge it's possible that it could be POPG but we know that R-phosphate interactions are also pretty strong

- Lipid 1: Charged: R88, Polar + Pi: Y27, Polar: N30
    - We have patch clamp data showing not much change in gating parameters when we mutate R88 and Y27 – I'd like to include it and discuss (Figure 4, Supplemental Figure 13)
    - Also G41A, I77G, F80A, F80S, G90A
- Lipid 2: Charged: R59, D67 (faces away from headgroup), Polar + Pi: Y75
    - We also have patch data for R59 and D67 (Figure 4, Supplemental Figure 13)
    - Also L72S, G76A, F68L, F68S, A103L, A103S, G104S, V107S
- Lipid 3: Charged: R59, K60, Polar + Pi: Y75
    - And patch data for K60 (Figure 4, Supplemental Figure 13)
    - Also L69D, L69N, L69H, L69S, A102S,
- Lipid 4: Charged: D67, Polar: T64, Q149 – I think this is probably a POPE
    - Also V65S, A106V, A106T, L11M, L111A, L111S, L115A, L115S, L115T, V122G, F151R, F151D F151A

Multiple nonpolar contacts between hydrophobic residues and the aliphatic chains (Supplemental Table 3)

Discussion

In situ MscS is sensitive to relatively small tensions. It inactivates in the 5-7 mN/m range and opens between 6 and 10 mN/m. Therefore, physical factors such as lateral pressure of lipids in the surrounding bilayer or Laplace pressure of the detergent micelle may easily influence its conformation. Polymers provide a critical advantage over traditional detergents and tend to preserve some associated lipids in their native positions. As shown by the liposome-like 2D classes (Supplemental Figure 15), the polymer is capable of excising large patches of native membrane with incorporated proteins. The conformation solved in Glyco-DIBMA is similar to previously reported structures (Bass et al., 2002; Flegler et al., 2021; Rasmussen et al., 2019a; Reddy et al., 2019). It belongs to the initial splayed class of structures (2OAU) with the gate uncoupled from the peripheral tension-sensing helical pairs. We observe a lack of ordered structure at the N-terminus before residue 17 that was previously reported (Reddy et al., 2019), but reproduce the presence of lipid 1 clinging to R88 (Rasmussen et al., 2019a; Reddy et al., 2019) and demonstrate new densities for lipids 2-4. We have identified the polar and non-polar interactions that stabilize these lipids non-bilayer positions. The structure most likely represents the non-conductive and tension-insensitive state where lipids stabilize the uncoupled state of the gate. Previous attempts to open this type of structure by applying cyclodextrins to nanodiscs (Zhang et al., 2021) or applying tension in coarse-grained and atomistic simulations (ref) failed to reopen this structure. The structure that would satisfy the conductive properties of open MscS has not been achieved. What positive mechanistic information can be extracted from the presented structures? First, these are volumes of interhelical crevices (spaces) occupied and stabilized by lipids. These volumes, when compared to volumes taken by lipids in a regular bilayer, are important parameters for computations of thermodynamic tendencies for the complex to compact or expand under lateral pressure or tension. We expect to find conditions and physical forces that would expel these non-bilayer lipids from the crevices as the TM2 and TM3 helices must establish physical contact to transmit tension from the lipid-facing helices to the gate (Belyy et al., 2010a). The identified lipid-stabilizing interactions with the protein will be targeted by the mutagenesis, and the channel versions that accommodate lipids more or less stably will be tested in functional experiments. The structures will be used as experimentally determined starting conformations for molecular simulations. This work opens multiple opportunities for functional and structural studies of MscS expressed in strains with altered lipid composition and identification of lipid species affecting opening or inactivation pathways.

Acknowledgements

We thank Joshua Zimmerberg and Jennifer Peterson for access to the Tecnai T20 Microscope and Wyatt Peele, Mario Borgnia, AJ Morton, Zabrina Lang, and Rick Huang for the support on the Krios. We are grateful to Samantha Miller for providing the MJF465 strain, Manuela Zoonens for providing the CyclAPol polymer, Gerald Kidd for assistance in membrane isolation, and Andriy Anishkin, Alex Sodt, and Louis Tung Faat Lai for valuable discussions. The research was supported by the Division of Intramural Research of the *Eunice Kennedy Shriver* National Institute of Child Health and Human Development, NIH (grant NICHD intramural projects Z1A HD008998 to DM). This work was supported by NIH R01-AI135015 to SS. This material is based upon work supported by the National Science Foundation Graduate Research Fellowship Program to EM under Grant No. DGE 1840340. Any opinions, findings, and conclusions or recommendations expressed in this material are those of the author(s) and do not necessarily reflect the views of the National Science Foundation.This work utilized the computational resources of the NIH HPC Biowulf cluster. (http://hpc.nih.gov). Molecular graphics and analyses performed with UCSF ChimeraX, developed by the Resource for Biocomputing, Visualization, and Informatics at UCSF, with support from NIH R01-GM129325 and the Office of Cyber Infrastructure and Computational Biology, NIAID.

References

Angiulli, G., H.S. Dhupar, H. Suzuki, I.S. Wason, F. Duong Van Hoa, and T. Walz. 2020. New approach for membrane protein reconstitution into peptidiscs and basis for their adaptability to different proteins. eLife. 9:e53530.

Bass, R.B., P. Strop, M. Barclay, and D.C. Rees. 2002. Crystal structure of Escherichia coli MscS, a voltage-modulated and mechanosensitive channel. Science. 298:1582-1587.

Belyy, V., A. Anishkin, K. Kamaraju, N. Liu, and S. Sukharev. 2010a. The tension-transmitting 'clutch' in the mechanosensitive channel MscS. Nat.Struct.Mol.Biol. 17:451-458.

Belyy, V., K. Kamaraju, B. Akitake, A. Anishkin, and S. Sukharev. 2010b. Adaptive behavior of bacterial mechanosensitive channels is coupled to membrane mechanics. J Gen Physiol. 135:641-652.

Corey, R.A., W. Song, A.L. Duncan, T.B. Ansell, M.S.P. Sansom, and P.J. Stansfeld. 2021. Identification and assessment of cardiolipin interactions with E. coli inner membrane proteins. Sci Adv. 7.

Danielczak, B., M. Rasche, J. Lenz, E. Pérez Patallo, S. Weyrauch, F. Mahler, M.T. Agbadaola, A. Meister, J.O. Babalola, C. Vargas, C. Kolar, and S. Keller. 2022. A bioinspired glycopolymer for capturing membrane proteins in native-like lipid-bilayer nanodiscs. Nanoscale. 14:1855-1867.

Flegler, V.J., A. Rasmussen, K. Borbil, L. Boten, H.-A. Chen, H. Deinlein, J. Halang, K. Hellmanzik, J. Löffler, V. Schmidt, C. Makbul, C. Kraft, R. Hedrich, T. Rasmussen, and B. Böttcher. 2021. Mechanosensitive channel gating by delipidation. Proceedings of the National Academy of Sciences. 118:e2107095118.

Flegler, V.J., T. Rasmussen, and B. Böttcher. 2022. How Functional Lipids Affect the Structure and Gating of Mechanosensitive MscS-like Channels. International Journal of Molecular Sciences. 23:15071.

Grant, T., A. Rohou, and N. Grigorieff. 2018. cisTEM, user-friendly software for single-particle image processing. Elife. 7.

Higgins, A.J., A.J. Flynn, A. Marconnet, L.J. Musgrove, V.L.G. Postis, J.D. Lippiat, C.-w. Chung, T. Ceska, M. Zoonens, F. Sobott, and S.P. Muench. 2021. Cycloalkane-modified amphiphilic polymers provide direct extraction of membrane proteins for CryoEM analysis. Communications Biology. 4:1337.

Iscla, I., R. Wray, and P. Blount. 2008. On the structure of the N-terminal domain of the MscL channel: helical bundle or membrane interface. Biophys J. 95:2283-2291.

Knowles, T.J., R. Finka, C. Smith, Y.-P. Lin, T. Dafforn, and M. Overduin. 2009. Membrane Proteins Solubilized Intact in Lipid Containing Nanoparticles Bounded by Styrene Maleic Acid Copolymer. Journal of the American Chemical Society. 131:7484-7485.

Levina, N., S. Totemeyer, N.R. Stokes, P. Louis, M.A. Jones, and I.R. Booth. 1999. Protection of Escherichia coli cells against extreme turgor by activation of MscS and MscL mechanosensitive channels: identification of genes required for MscS activity. EMBO J. 18:1730-1737.

Liebschner, D., P.V. Afonine, M.L. Baker, G. Bunkóczi, V.B. Chen, T.I. Croll, B. Hintze, L.W. Hung, S. Jain, A.J. McCoy, N.W. Moriarty, R.D. Oeffner, B.K. Poon, M.G. Prisant, R.J. Read, J.S. Richardson, D.C. Richardson, M.D. Sammito, O.V. Sobolev, D.H. Stockwell, T.C. Terwilliger, A.G. Urzhumtsev, L.L. Videau, C.J. Williams, and P.D. Adams. 2019. Macromolecular structure determination using X-rays, neutrons and electrons: recent developments in Phenix. Acta Crystallogr D Struct Biol. 75:861-877.

Marconnet, A., B. Michon, C. Le Bon, F. Giusti, C. Tribet, and M. Zoonens. 2020. Solubilization and Stabilization of Membrane Proteins by Cycloalkane-Modified Amphiphilic Polymers. Biomacromolecules. 21:3459-3467.

Marconnet, A., B. Michon, B. Prost, A. Solgadi, C. Le Bon, F. Giusti, C. Tribet, and M. Zoonens. 2022. Influence of Hydrophobic Groups Attached to Amphipathic Polymers on the Solubilization of Membrane Proteins along with Their Lipids. Analytical Chemistry. 94:14151-14158.

Mastronarde, D.N. 2005. Automated electron microscope tomography using robust prediction of specimen movements. J Struct Biol. 152:36-51.

Nomura, T., M. Sokabe, and K. Yoshimura. 2006. Lipid-protein interaction of the MscS mechanosensitive channel examined by scanning mutagenesis. Biophys J. 91:2874-2881.

Notti, R.Q., and T. Walz. 2022. Native-like environments afford novel mechanistic insights into membrane proteins. Trends in Biochemical Sciences. 47:561-569.

Park, Y.C., B. Reddy, N. Bavi, E. Perozo, and J.D. Faraldo-Gómez. 2023. State-specific morphological deformations of the lipid bilayer explain mechanosensitive gating of MscS ion channels. eLife. 12:e81445.

Pliotas, C., A.C. Dahl, T. Rasmussen, K.R. Mahendran, T.K. Smith, P. Marius, J. Gault, T. Banda, A. Rasmussen, S. Miller, C.V. Robinson, H. Bayley, M.S. Sansom, I.R. Booth, and J.H. Naismith. 2015. The role of lipids in mechanosensation. Nat Struct Mol Biol. 22:991-998.

Pliotas, C., R. Ward, E. Branigan, A. Rasmussen, G. Hagelueken, H. Huang, S.S. Black, I.R. Booth, O. Schiemann, and J.H. Naismith. 2012. Conformational state of the MscS mechanosensitive channel in solution revealed by pulsed electron-electron double resonance (PELDOR) spectroscopy. Proc Natl Acad Sci U S A. 109:E2675-2682.

Punjani, A., J.L. Rubinstein, D.J. Fleet, and M.A. Brubaker. 2017. cryoSPARC: algorithms for rapid unsupervised cryo-EM structure determination. Nature Methods. 14:290-296.

Punjani, A., H. Zhang, and D.J. Fleet. 2020. Non-uniform refinement: adaptive regularization improves single-particle cryo-EM reconstruction. Nature Methods. 17:1214-1221.

Qiu, W., Z. Fu, G.G. Xu, R.A. Grassucci, Y. Zhang, J. Frank, W.A. Hendrickson, and Y. Guo. 2018. Structure and activity of lipid bilayer within a membrane-protein transporter. Proceedings of the National Academy of Sciences. 115:12985-12990.

Rasmussen, T., V.J. Flegler, A. Rasmussen, and B. Böttcher. 2019a. Structure of the Mechanosensitive Channel MscS Embedded in the Membrane Bilayer. Journal of Molecular Biology. 431:3081-3090.

Rasmussen, T., A. Rasmussen, L. Yang, C. Kaul, S. Black, H. Galbiati, S.J. Conway, S. Miller, P. Blount, and I.R. Booth. 2019b. Interaction of the Mechanosensitive Channel, MscS, with the Membrane Bilayer through Lipid Intercalation into Grooves and Pockets. Journal of Molecular Biology. 431:3339-3352.

Reddy, B., N. Bavi, A. Lu, Y. Park, and E. Perozo. 2019. Molecular basis of force-from-lipids gating in the mechanosensitive channel MscS. Elife. 8.

Rohou, A., and N. Grigorieff. 2015. CTFFIND4: Fast and accurate defocus estimation from electron micrographs. J Struct Biol. 192:216-221.

Sotomayor, M., and K. Schulten. 2004. Molecular dynamics study of gating in the mechanosensitive channel of small conductance MscS. Biophys.J. 87:3050-3065.

Sukharev, S. 2002. Purification of the Small Mechanosensitive Channel of Escherichia coli (MscS): the Subunit Structure, Conduction, and Gating Characteristicsin Liposomes. Biophysical Journal. 83:290-298.

Sun, C., S. Benlekbir, P. Venkatakrishnan, Y. Wang, S. Hong, J. Hosler, E. Tajkhorshid, J.L. Rubinstein, and R.B. Gennis. 2018. Structure of the alternative complex III in a supercomplex with cytochrome oxidase. Nature. 557:123-126.

Vásquez, V., M. Sotomayor, J. Cordero-Morales, K. Schulten, and E. Perozo. 2008a. A structural mechanism for MscS gating in lipid bilayers. Science. 321:1210-1214.

Vásquez, V., M. Sotomayor, D.M. Cortes, B. Roux, K. Schulten, and E. Perozo. 2008b. Three-dimensional architecture of membrane-embedded MscS in the closed conformation. J Mol Biol. 378:55-70.

Wang, W., S.S. Black, M.D. Edwards, S. Miller, E.L. Morrison, W. Bartlett, C. Dong, J.H. Naismith, and I.R. Booth. 2008. The structure of an open form of an E. coli mechanosensitive channel at 3.45 A resolution. Science. 321:1179-1183.

Zhang, Y., C. Daday, R.-X. Gu, C.D. Cox, B. Martinac, B.L. de Groot, and T. Walz. 2021. Visualization of the mechanosensitive ion channel MscS under membrane tension. Nature. 590:509-514.

Zheng, S.Q., E. Palovcak, J.-P. Armache, K.A. Verba, Y. Cheng, and D.A. Agard. 2017. MotionCor2: anisotropic correction of beam-induced motion for improved cryo-electron microscopy. Nature Methods. 14:331-332.

Zhu, L., W. Zhao, Y. Yan, X. Liao, A. Bourtsalas, Y. Dan, H. Xiao, and X. Chen. 2020. Interaction between mechanosensitive channels embedded in lipid membrane. Journal of the Mechanical Behavior of Biomedical Materials. 103:103543.

Figures and Tables

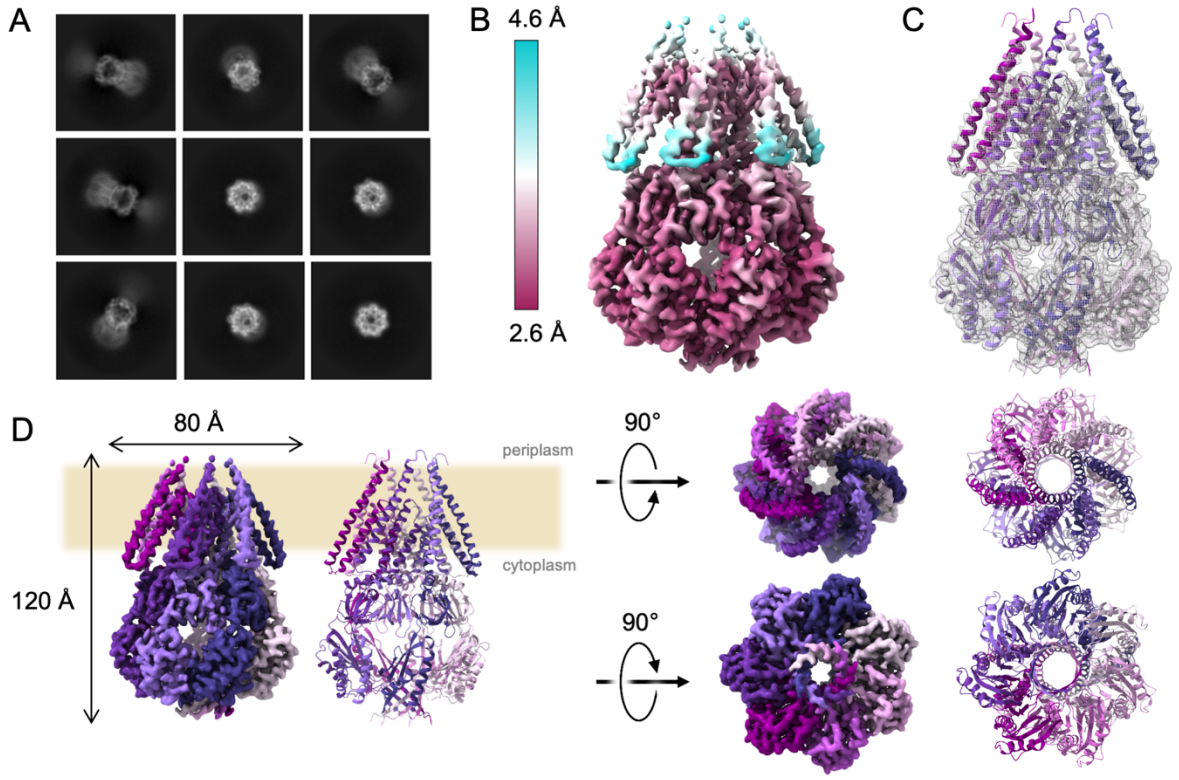

Figure 1: MscS Structure in Glyco-DIBMA. (A) Selected 2D class averages of the particles used for the final reconstruction. (B) Cryo-EM map colored by local resolution (C) Fitted model inside map shown in mesh. (D) Map and model colored by chain side view, top view, and bottom view with dimensions shown on the left and the membrane region highlighted in yellow.

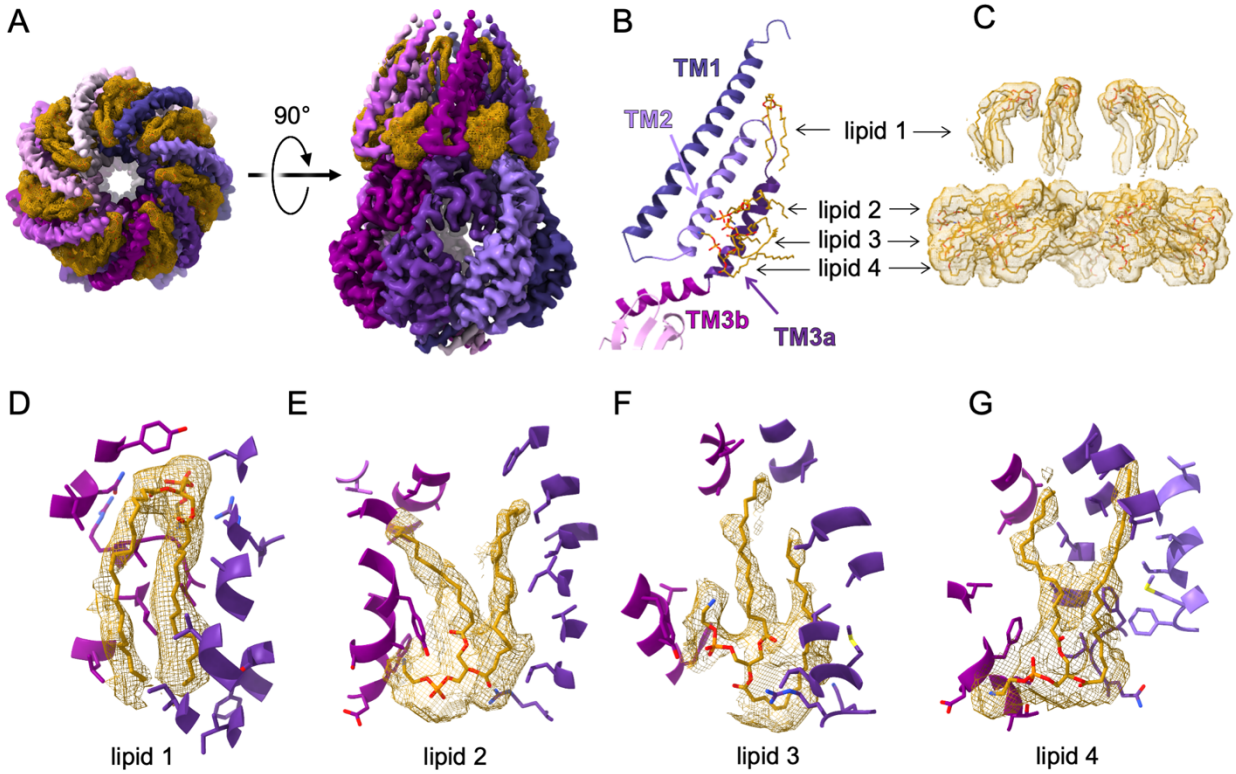

Figure 2: Lipids. (A) Map colored by chain top view and side view with lipid densities shown in yellow. (B) Protein monomer colored by domain with the locations of modelled lipids. (C) Side view of lipid densities shown in mesh with modelled lipids inside. (D) Zoomed in view of lipid 1 with mesh density shown with all residues within 5 Å in the modelled protein. (E) Zoomed in view of lipid 2 with mesh density shown with all residues within 5 Å in the modelled protein. (F) Zoomed in view of lipid 3 with mesh density shown with all residues within 5 Å in the modelled protein. (G) Zoomed in view of lipid 4 with mesh density shown with all residues within 5 Å in the modelled protein.

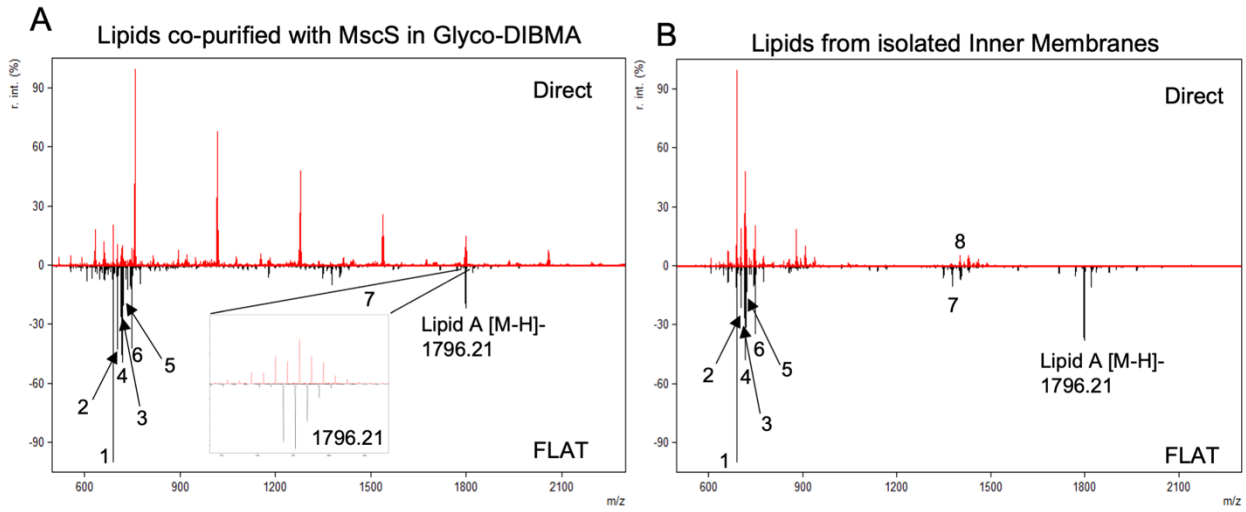

Figure 3: Lipid Mass Spectrometry. (A) Lipids co-purified with MscS in Glyco-DIBMA. (B) Lipids from isolated Inner Membranes.

Table 1: Relative quantification of lipids.

Number	Matched Mass	Name	Formula	Relative Intensity (MscS in Glyco-DIBMA : Inner Membranes)
1	688.49	PE 32:1	C37H72NO8P	100:100
2	702.51	PE 33:1	C38H74NO8P	42:21
3	714.51	PE 34:2	C39H74NO8P	26:26
4	716.52	PE 34:1	C39H76NO8P	46:48
5	719.49	PG 32:1	C38H73O10P	50:31
6	747.52	PG 34:1	C40H77O10P	43:34
7	1375.97	CL 66:2	C75H142O17P2	10:10
8	1796.21	Lipid A	C94H178N2O25P2	19:36

Supplementary Information

Polymer-solubilized structures suggest the role of protein-lipid interactions in the functional gating cycle of the mechanosensitive channel MscS

Elissa Moller [1,2,3], Madolyn Britt [2,3], Fei Zhou [1], Hyojik Yang [5], Robert Ernst [5], Sergei Sukharev [2,3,4,#], Doreen Matthies [1,#]

[1] Unit on Structural Biology, Division of Basic and Translational Biophysics, *Eunice Kennedy Shriver* National Institute of Child Health and Human Development, National Institutes of Health, Bethesda, MD, USA.
[2] Biophysics Graduate Program, University of Maryland, College Park, MD, USA.
[3] Department of Biology, University of Maryland, College Park, MD, USA.
[4] Institute for Physical Science and Technology, University of Maryland, College Park, MD, USA.
[5] Department of Microbial Pathogenesis, University of Maryland, Baltimore, MD, USA.
[6] Biochemistry and Molecular Biology, University of Texas Medical School, Houston, TX, USA.

Correspondence to Sergei Sukharev (sukharev@umd.edu) and Doreen Matthies (Doreen.Matthies@nih.gov)

Supplemental Figure 1: Membrane protein extraction methods.
Supplemental Figure 2: Negative Staining of Polymers.
Supplemental Figure 3: Glyco-DIBMA biochemical characterization and negative staining EM.
Supplemental Figure 4: SMA200/SMALP biochemical characterization and negative staining EM.
Supplemental Figure 5: CyclAPol biochemical characterization and negative staining EM.
Supplemental Figure 6: Glyco-DIBMA #1 cryo-EM workflow.
Supplemental Figure 7: Glyco-DIBMA #2 cryo-EM workflow.
Supplemental Figure 8: SMA200/SMALP #1 cryo-EM workflow.
Supplemental Figure 9: SMA200/SMALP #2 cryo-EM workflow.
Supplemental Figure 10: CyclAPols cryo-EM workflow.
Supplemental Figure 11: Quality of the cryo-EM map and fitted model of MscS in Glyco-DIBMA.
Supplemental Figure 12: Extra Densities of MscS in Glyco-DIBMA.

Supplemental Table 1: Cryo-EM data collection parameters and analysis.
Supplemental Table 2: Cryo-EM map and model analysis.
Supplemental Table 3: Residues within 5 Å of modelled lipids.

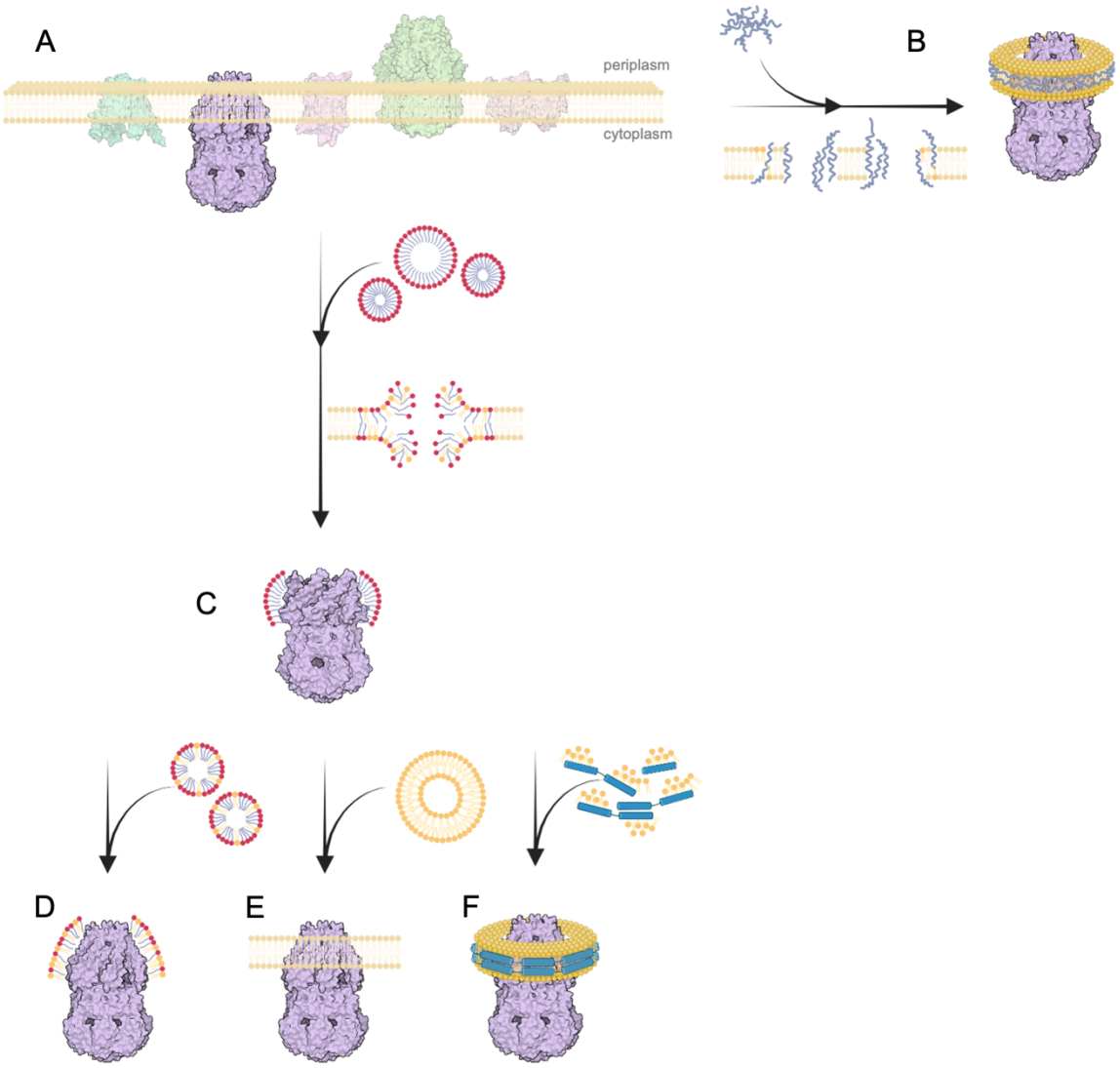

Supplemental Figure 1: Membrane protein extraction methods. (A) Membrane proteins in the bilayer. (B) Direct membrane solubilization using polymers. (C) Detergent solubilization. (D) Addition of lipids to form mixed micelles. (E) Reconstitution into liposomes. (F) Reconstitution into nanodiscs.

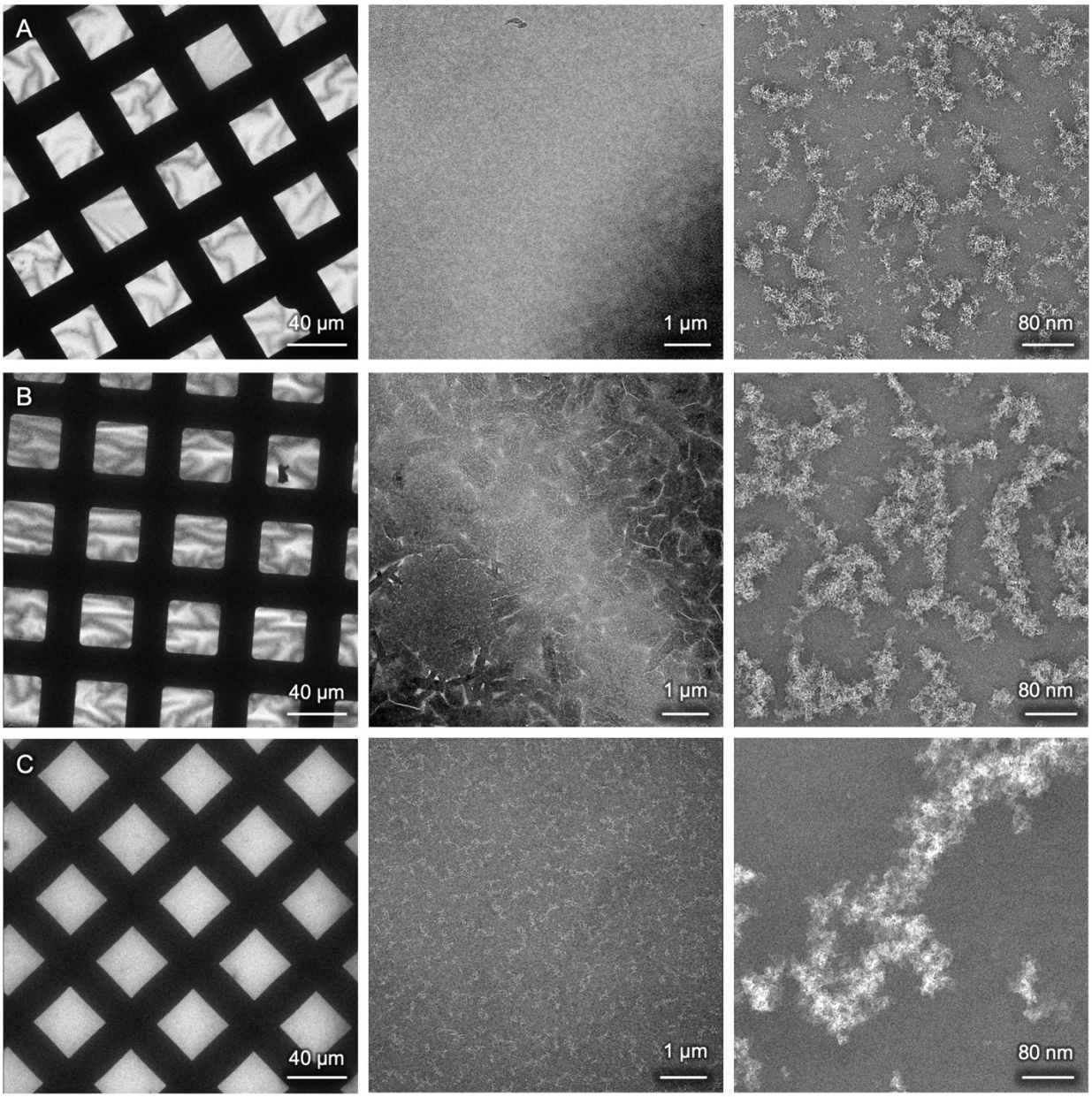

Supplemental Figure 2: Negative Staining of Polymers. (A) 0.5% Glyco-DIBMA in HEPES buffer at low magnification (left) medium magnification (middle) and high magnification (right). (B) 1% SMALP 200 in Tris buffer at low magnification (left) medium magnification (middle) and high magnification (right). (C) 0.1% CyclAPols in Tris buffer at low magnification (left) medium magnification (middle) and high magnification (right).

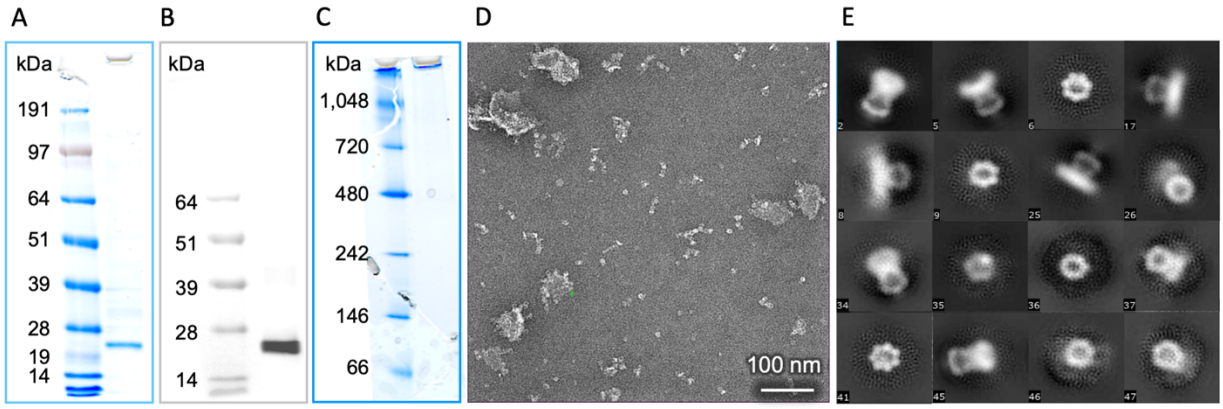

Supplemental Figure 3: Glyco-DIBMA biochemical characterization and negative staining EM. (A) SDS Gel (B) Western Blot (C) BN Gel (D) Micrograph (E) Selected 2D class averages.

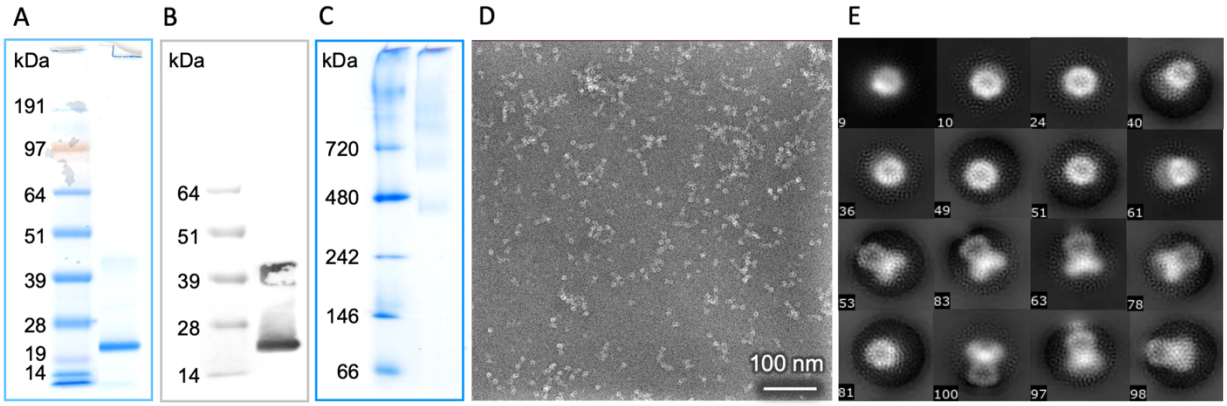

Supplemental Figure 4: SMA200/SMALP biochemical characterization and negative staining EM. (A) SDS Gel (B) Western Blot (C) BN Gel (D) Micrograph (E) Selected 2D class averages.

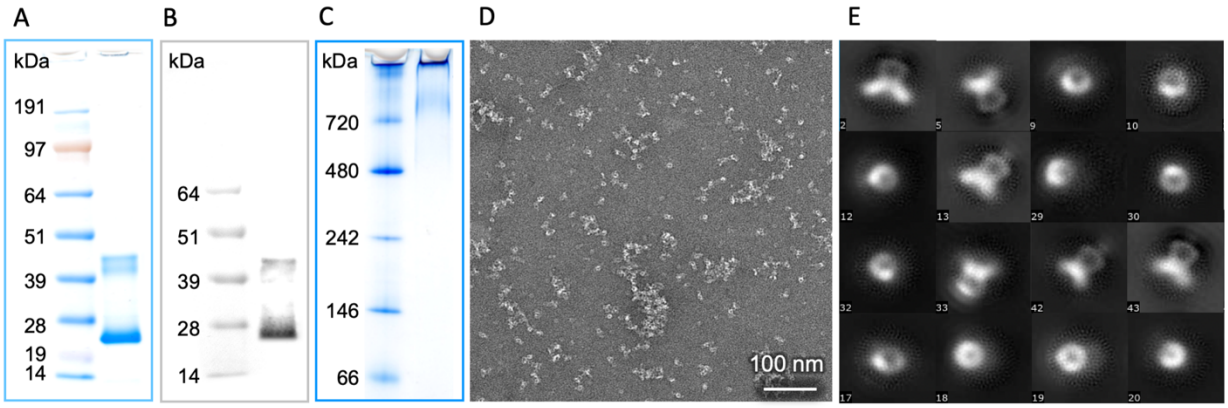

Supplemental Figure 5: CyclAPol biochemical characterization and negative staining EM. (A) SDS Gel (B) Western Blot (C) BN Gel (D) Micrograph (E) Selected 2D class averages.

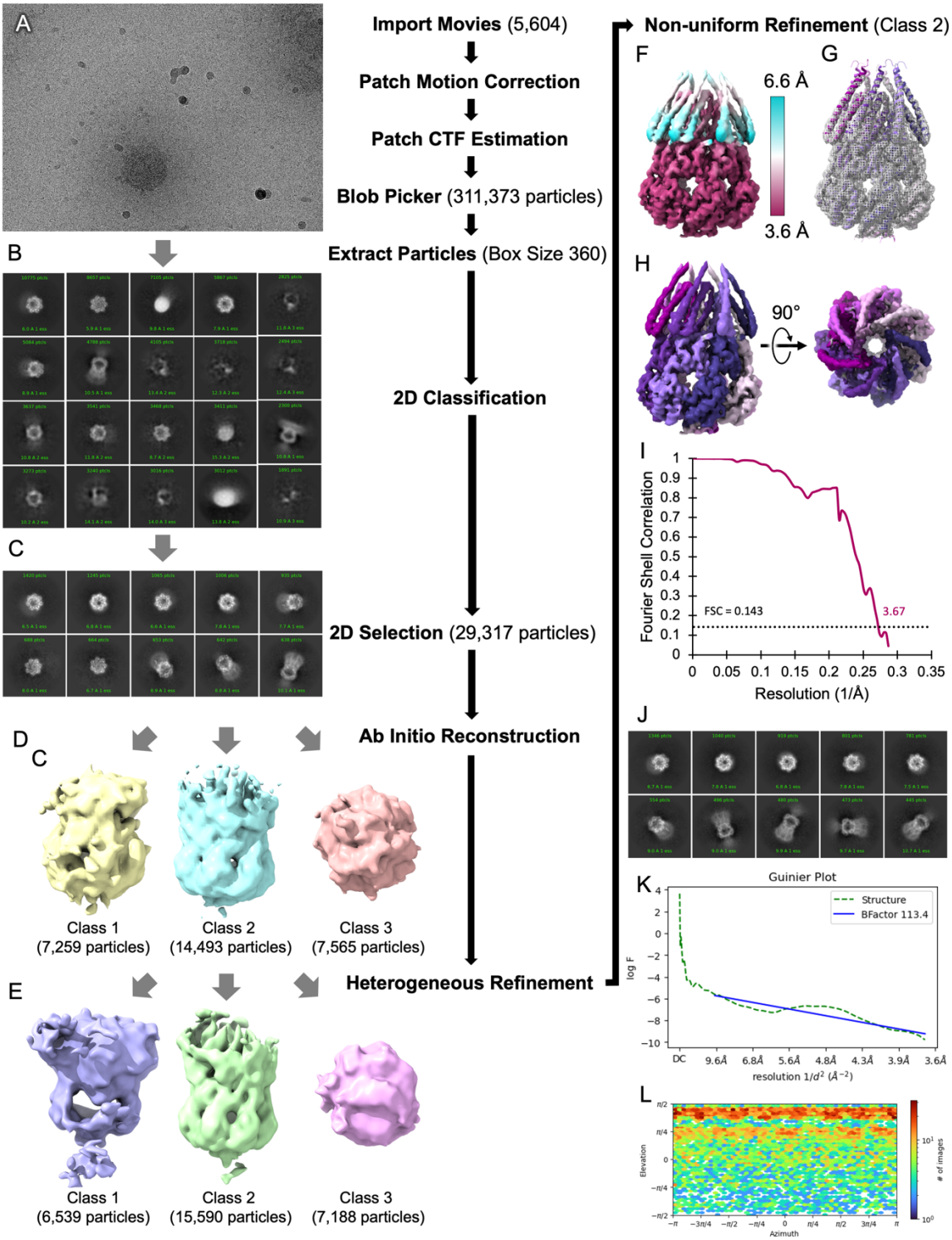

Supplemental Figure 6: Glyco-DIBMA #1 cryo-EM workflow. (A) Micrograph (B) Representative 2D class averages from the initial particle picking. (C) Selected 2D class averages used for Ab Initio Reconstruction. (D) Ab Initio Models (E) Heterogeneous Refinement (F) Non-uniform refinement of Class 2 (Supplemental Figure 6E) with C7 symmetry colored by local resolution. (G) MscS model rigid body fit to map shown in mesh. (H) Map colored by chain side view and top view. (I) FSC curve. (J) Representative 2D class averages used for final reconstruction. (K) Guinier Plot. (L) Viewing Directions.

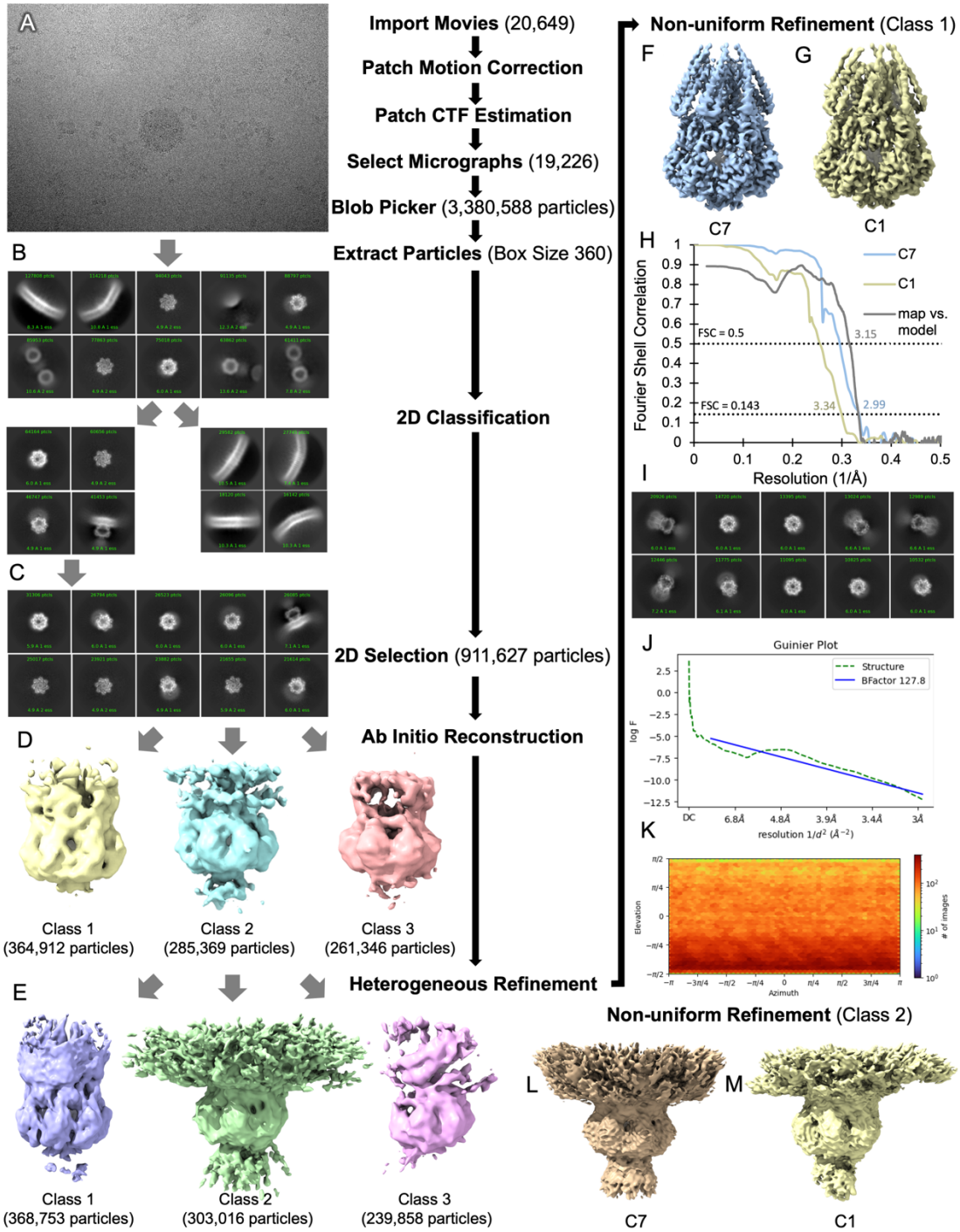

Supplemental Figure 7: Glyco-DIBMA #2 cryo-EM workflow. (A) Micrograph (B) Representative 2D class averages from the initial particle picking. (C) Selected 2D class averages used for Ab Initio Reconstruction. (D) Ab Initio Models (E) Heterogeneous Refinement (F) Non-uniform refinement of Class 1 (Supplemental Figure 7E) with C7 symmetry. (G) Non-uniform refinement of Class 1 (Supplemental Figure 7E) with C1 symmetry. (H) FSC curve for C7 (blue), C1 (yellow), and map vs. model (gray). (I) Representative 2D class averages used for final reconstruction. (J) Guinier Plot. (K) Viewing Directions. (L) Non-uniform refinement for Class 2 (Supplemental Figure 7E) with C7 symmetry. (M) Non-uniform refinement for Class 2 (Supplemental Figure 7E) with C1 symmetry.

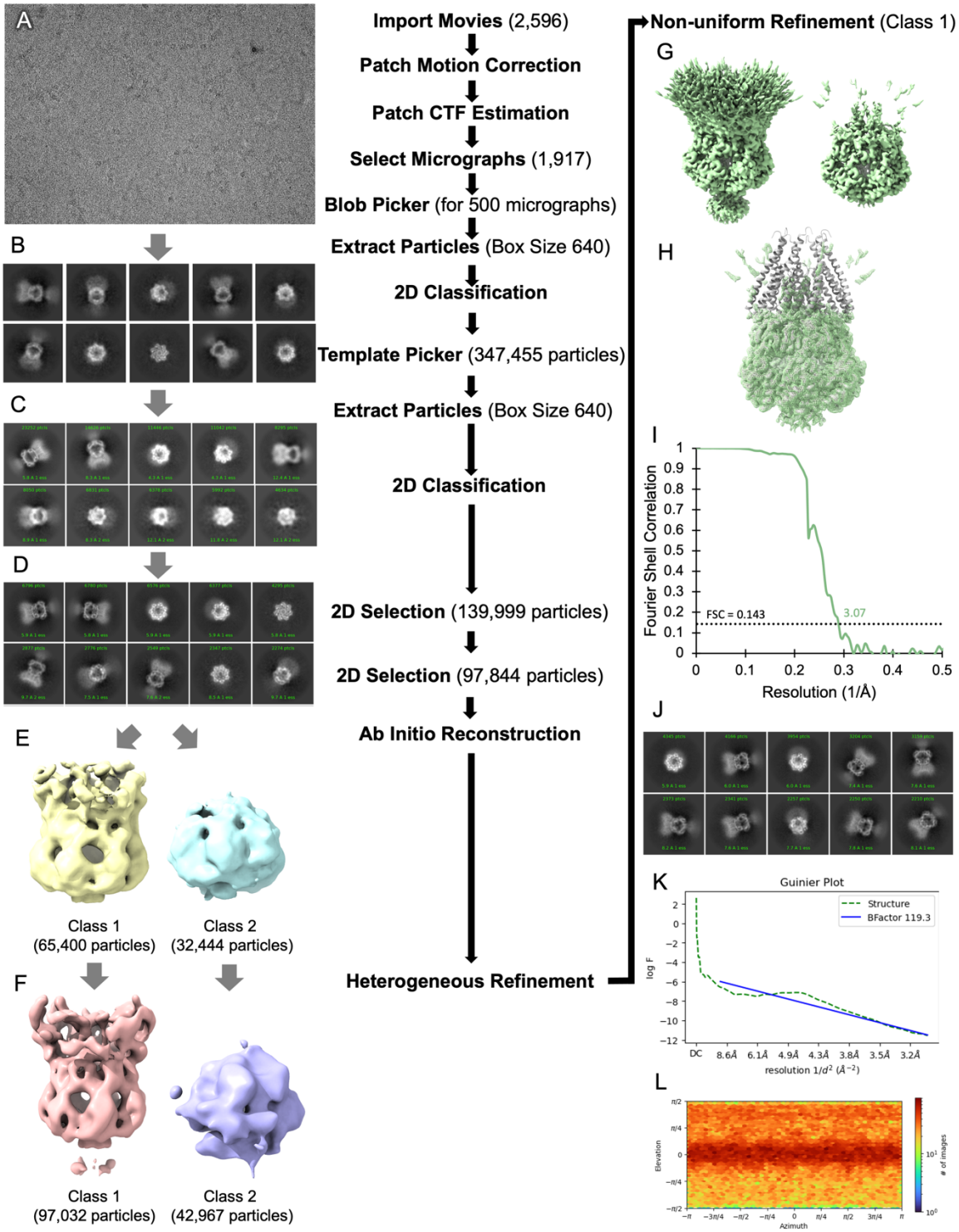

Supplemental Figure 8: SMA200/SMALP #1 cryo-EM workflow. (A) Micrograph (B) Representative 2D class averages from the initial particle picking. (C) Selected 2D class averages. (D) 2D class averages used for Ab Initio Reconstruction. (E) Ab Initio Models (F) Heterogeneous Refinement (G) Non-uniform refinement of Class 1 (Supplemental Figure 8F) with C7 symmetry at different thresholds. (H) MscS model rigid body fit to map shown in mesh. (I) FSC curve. (J) Representative 2D class averages used for final reconstruction. (K) Guinier Plot. (L) Viewing Directions.

Supplemental Figure 9: SMA200/SMALP #2 cryo-EM workflow.

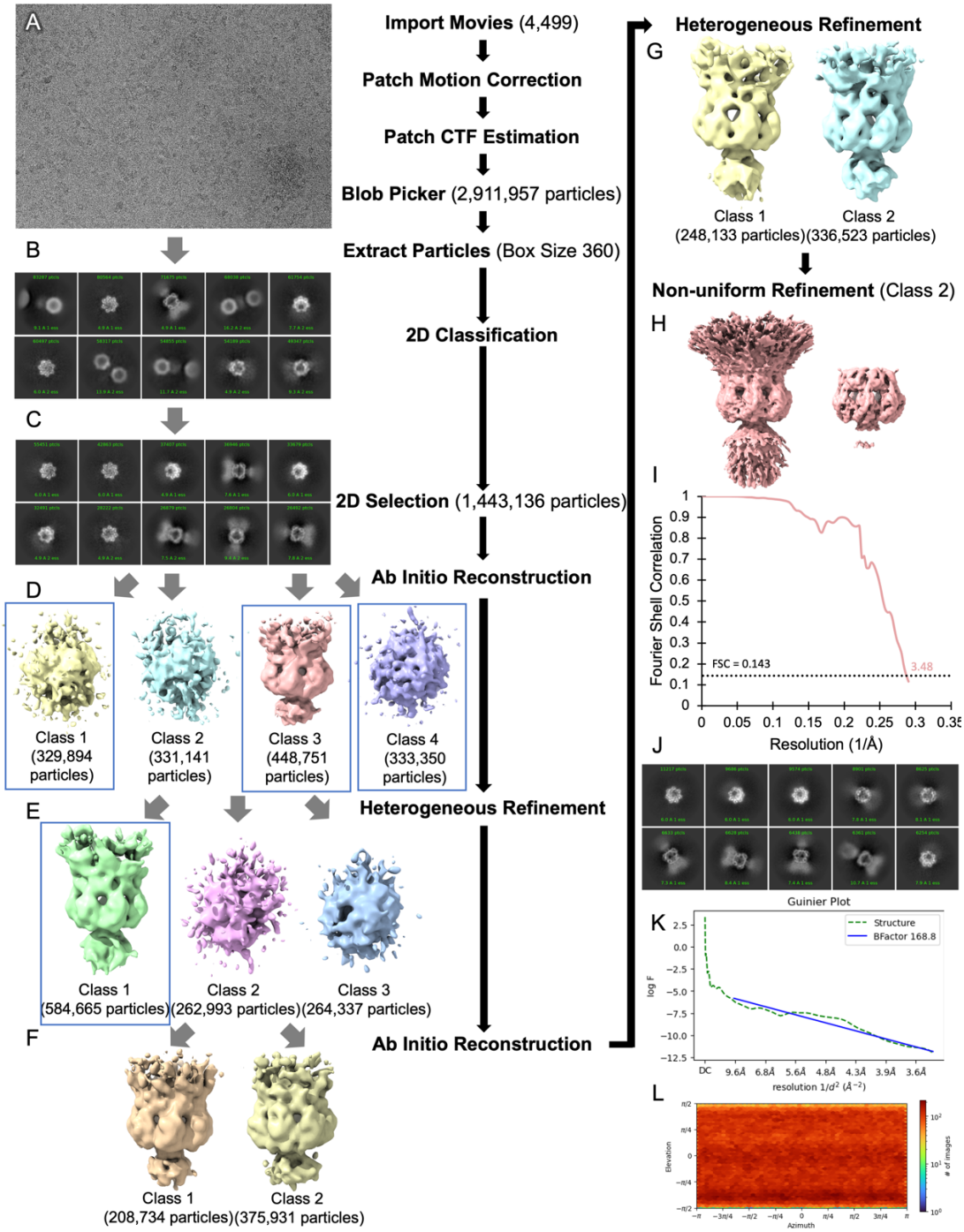

Supplemental Figure 10: CyclAPols cryo-EM workflow. (A) Micrograph (B) Representative 2D class averages from the initial particle picking. (C) Selected 2D class averages used for Ab Initio Reconstruction. (D) Initial Ab Initio Models, particles and maps in blue boxes were used for the following heterogeneous refinement (Supplemental Figure 10E). (E) Heterogeneous Refinement of selected particles and maps from ab initio reconstruction (Supplemental Figure 10D), particles and map in the blue box were subjected to another round of ab initio reconstruction (Supplemental Figure 10F). (F) Second round of Ab Initio Reconstruction. (G) Heterogeneous Refinement (H) Non-uniform refinement of Class 2 (Supplemental Figure 10G) with C7 symmetry at different thresholds. (I) FSC curve. (J) Representative 2D class averages used for final reconstruction. (K) Guinier Plot. (L) Viewing Directions.

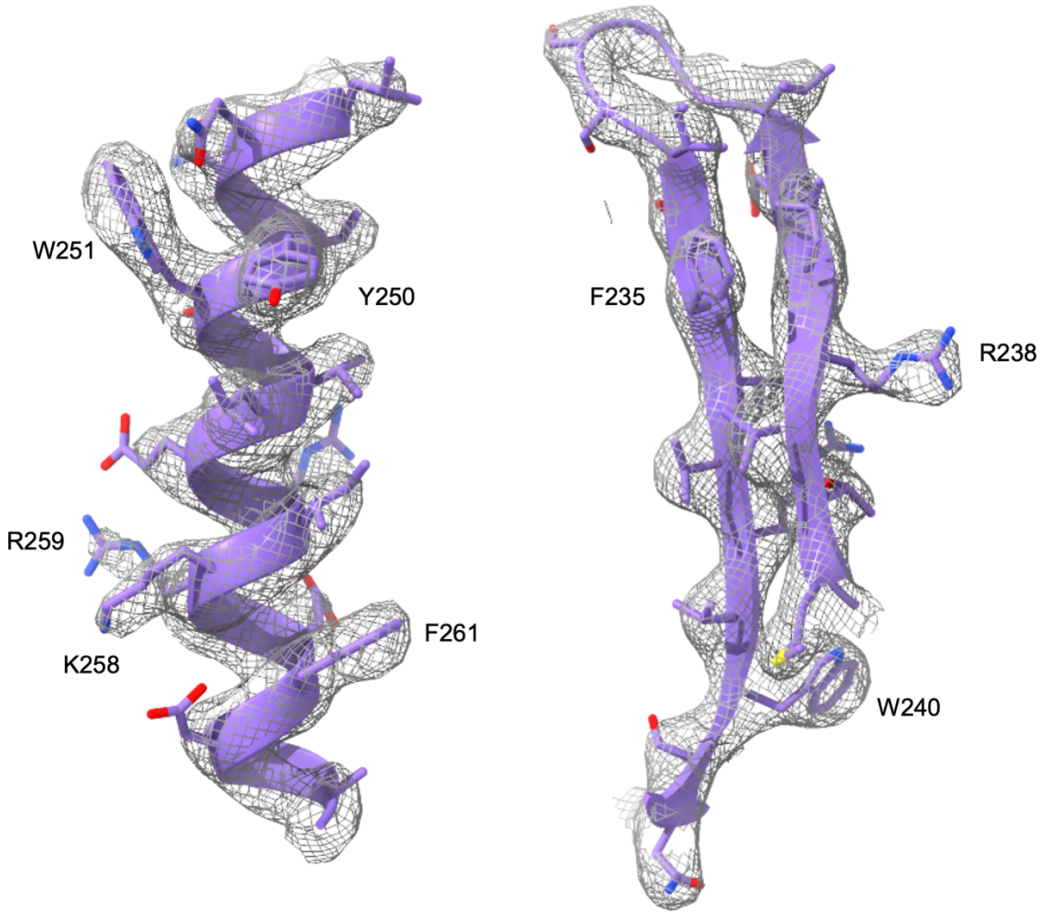

Supplemental Figure 11: Quality of the cryo-EM map and fitted model of MscS in Glyco-DIBMA. Representative densities of an α-helix (left) and a β-sheet (right).

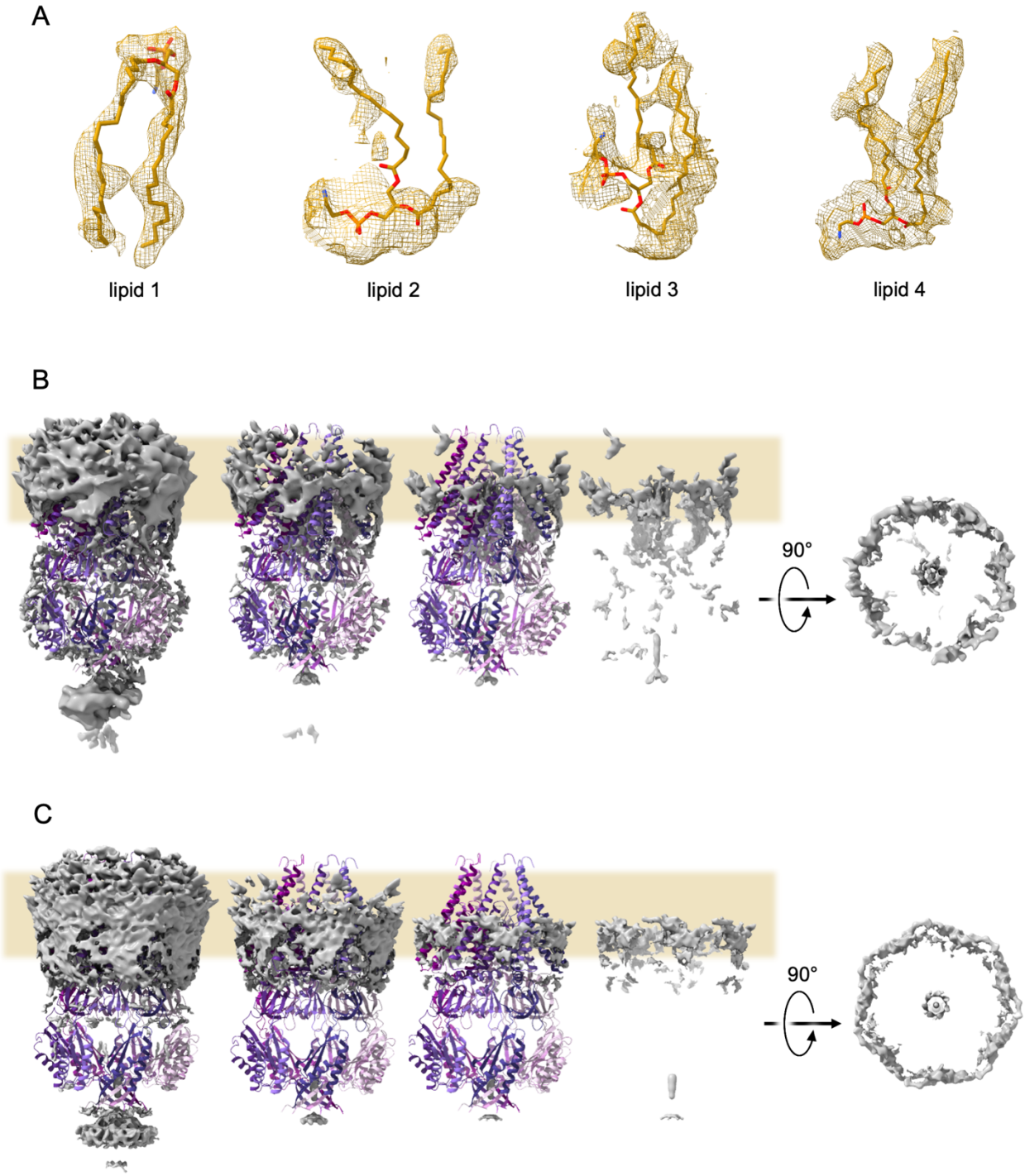

Supplemental Figure 12: Extra Densities of MscS in Glyco-DIBMA. (A) Lipids 1-4 in C1 symmetry. (B) Additional densities not modelled as lipids in C1 symmetry at varying thresholds. (C) Additional densities not modelled as lipids in C7 symmetry at varying thresholds.

Supplemental Table 1: Cryo-EM data collection parameters and analysis.

	Glyco-DIBMA #1	Glyco-DIBMA #2	SMALP 200 #1	SMALP 200 #2	CyclAPol C_8-C_0-50
Date of collection	10/3/23	11/9/23	5/9/23	5/23/23	10/4/23
Protein concentration	0.1 mg/mL	0.3 mg/mL	0.3 mg/mL	0.4 mg/mL	0.7 mg/mL
Sample volume	3 µl	3 µl	3 µl	3 µl	3 µl
Double Blot	yes	yes	no	no	no
Grid type	QF R 1.2/1.3 400 Cu mesh + 2nm C	QF R 1.2/1.3 400 Cu mesh + 2nm C	QF R 1.2/1.3 400 Cu mesh + 2nm C	QF R 1.2/1.3 400 Cu mesh + 2nm C	QF R 1.2/1.3 400 Cu mesh + 2nm C
Plunge freezer	Leica EM GP2	Leica EM GP2	Leica EM GP2	Leica EM GP2	Leica EM GP2
Blotting time (s)	6	6	6	6	6
Temperature (°C)	4	4	4	4	4
Humidity (set)	95%	95%	95%	95%	95%
Microscope	Titan Krios G4	Titan Krios G4	Titan Krios G4	Titan Krios G1	Titan Krios G4
Voltage (kV)	300	300	300	300	300
Camera	K3 (non-CDS mode)	K3 (non-CDS mode)	K3 (CDS mode)	K3 (CDS mode)	K3 (non-CDS mode)
Energy filter (slit)	Yes (20 eV)	Yes (20 eV)	Yes (20 eV)	Yes (20 eV)	Yes (20 eV)
Cs corrector	no	no	no	no	no
Objective aperture	no	no	no	100 µm	no
Magnification	105,000x	105,000x	105,000x	105,000x	105,000x
Physical pixel size (Å/px)	0.85	0.85	0.85 (0.425 super-resolution)	0.83 (0.415 super-resolution)	0.85
Electron exposure (e-/Å^2)	50	50	50	50	50
Number of movie frames	60	60	60	50	60
Dose rate (e-/px/s)	15	15	10	9	15
Defocus (µm)	-0.8 to -1.7	-0.8 to -1.7	-0.8 to -1.7	-0.8 to -1.8	-0.8 to -1.7
Number of total micrographs	5,604	20,649	2,597	3,100	4,654
Number of selected micrographs	5,604	19,226	1,917	2,937	4,654
Number of particles picked	311,373	3,380,588	47,038	1,177,470	2,911,957

Supplemental Table 2: Cryo-EM map and model analysis.

	Glyco-DIBMA #2 EMD-XXXX PDB ID: XXXX	Glyco-DIBMA #2 EMD-XXXX PDB ID: XXXX
Data processing		
Final number of particles	368,753	368,753
Final pixel size used for final maps (Å/px)	0.85	0.85
Symmetry imposed	C7	C1
Resolution of map (Å)	2.99	3.34
FSC threshold	0.143	0.143
B-factor for map ($Å^2$)	127.8	
Model composition		
Chains	7	7
Non-hydrogen atoms	15,512	15,512
Protein residues	1,855	1,855
Water	98	98
Ligands	28	28
Refinement and validation		
Model resolution (Å)	3.1	3.9
FSC threshold	0.5	0.5
Bond lengths RMSD (Å)	0.002	0.003
Bond angle RMSD (°)	0.441	0.580
MolProbity score	1.63	1.45
Clashscore	7.49	8.33
Rotamer outliers (%)	1.91	0.34
Ramachandran outliers (%)	0.00	0.00
Ramachandran favored (%)	98.48	98.48
Ramachandran allowed (%)	1.52	1.52

Supplemental Table 3: Residues within 5 Å of modelled lipids.

	Lipid 1	Lipid 2	Lipid 3	Lipid 4
Chain A	V29, A33, A36, I37, V40, G41, I44, I77, F80, T81, R88	I48, V52, L55, R59, L72, V73, G76, I77, F80	V52, L55, M56, R59, K60, L69, L72, V73, G104, V107, G108	L69, L72, V107, G108, L111, L115, L118, Q149, I150, F151
Chain B	Y27, N30, I31, L82, L86, R88, V89, G90, V91	D67, F68, S70, A71, L72, Y75, G76, A79, F80, L100, A103, G104, V107	F68, A71, L72, Y75, V99, A102, A103	T64, V65, D67, F68, L72, A103, A106, V107
Chain C		V99		
Chain G				L118, A119, V122, L123, M126, F110